ARTICLE OPEN

Formation of calcareous deposits in the tidal zone and its effect on cathodic protection

Caiqi Yao[1,2,5], Xinru Wang[3,5], Wei Zhang[1,2 ✉], Wenting Xia[1,2], Zhiwei Chen[1,2] and Bing Han[4]

Using the wire beam electrode technique, electrochemical impedance spectroscopy, energy-dispersive X-ray spectroscopy, the formation of calcareous deposits in a tidal zone and its effects on the corrosion and protection of Q235 steel under cathodic protection were studied. Results showed that the production of aragonite $CaCO_3$ crystals significantly reduced from the immersion zone to the high-tide zone, the protective performance of the deposited layer weakened, and the corrosion of the metal intensified. In the immersion zone, the cathodic protection current density decreased, and the potential shifted negatively, indicating that the protection performance of the deposited layer was enhanced and the metal was effectively protected. In the tidal zone, the deposited layer was stratified, and the porosity of the deposited layer increased by dry-wet cycling. During flood tide, the cathodic reaction is accelerated near the waterline, which promotes the corrosion of the metal and the loss of the sacrificial anode under water.

INTRODUCTION

The marine tidal zone refers to the seawater area between the average low tide and the average high tide[1,2]. Marine engineering structures installed in this region are simultaneously affected by periodic waves, ocean currents, dry-wet cycling, and other environmental factors, accelerating the deterioration of coatings and corrosion of base metals[3,4]. Furthermore, one of the typical environmental characteristics of the tidal zone is dynamic water-line effect[5,6]. Near the water-line, O_2 concentration cells are formed due to the difference in the solubility of O_2. The anodic reaction zone of the galvanic cell is corroded because of the low concentration of O_2 below the water-line, whereas the area near the water-line is protected as the cathode due to high concentration of O_2 in this area. However, the research results also show that the intermediate generated by the cathodic reduction of O_2 at the high water-line and high pH accelerate the stripping of the coating from the base metal surface and thereby the failure rate of the coating[7–9]. Water-line corrosion is a highly concentrated local corrosion[7,10], and the change in tide level promotes repeated corrosion in the entire tidal zone with tide floods and ebbs[3,11].

Dry-wet cycling is another typical environmental feature in the tidal zone. During the drying-wetting cycle, drying occurs when the corrosion process intensely changes[12,13]. Via Kelvin probe technology, it has been confirmed that thinning of the liquid layer during metal surface drying accelerates the rate of O_2 reduction cathode reaction and promotes corrosion[14,15]. In the case of the protective coating in the water-line area, the repeated water-absorbing expansion and water-losing contraction of the coating reduces the shielding performance of the coating and accelerates the infiltration of corrosive medium and dissolved O_2 into the coating/metal interface, thereby increasing the corrosion rate of the base metal[16].

The difficulty in implementing effective corrosion control is also an important reason for high metal corrosion in the tidal zone. Cathodic protection, which is efficient in the full immersion zone, cannot effectively protect the tidal zone from corrosion because of the lack of a necessary electrolyte solution. Results of the long scale test show that the higher the tide level, the higher the protection current from the immersion zone; nevertheless, the higher the tide level, the shorter the immersion time, and the lower the cathodic protection, which is the most serious reason for corrosion[1,17].

During cathodic protection in a seawater environment, the surface alkalinity of steel structure will form a deposited layer rich in $Mg(OH)_2$ and $CaCO_3$, whose function is similar to that of an insulation coating[18], which can efficiently reduce the rate of diffusion of dissolved O_2 to the surface of the steel structure, thus reducing the cathodic protection current density required to polarize the potential to the cathodic protection potential range[2,19,20]. Although the deposition layer is a by-product of cathodic protection, it plays a crucial role in reducing the current demand for cathodic protection[21–25].

Numerous studies have been performed globally on the formation mechanisms of Ca and Mg deposits[21–25], and a relatively consistent view has been established. The formation process of Ca and Mg deposits is as follows:

In seawater, the cathodic protection potential range of steel structure is −0.78 to −1.03 V (vs. SCE)[26,27]. The type of cathodic reduction reaction at the steel/seawater interface depends on polarisation potential[28,29]. When the polarisation potential is higher than −0.95 V (vs. SCE), O_2 absorption mainly occurs (Eq. (1)). When the polarisation potential is lower than −1.10 V (vs. SCE), the water reduction primarily takes place (Eq. (2)). Regardless of the kind of reduction reaction, the pH of the steel structure/ seawater interface increases[30]. If the pH reaches the critical value of 9.5, the OH^- generated by the cathodic reaction can deposit

[1]School of Chemical Engineering and Technology, Sun Yat-sen University, Zhuhai 519082, China. [2]Southern Marine Science and Engineering Guangdong Laboratory (Zhuhai), Zhuhai 519082, China. [3]School of Materials, Sun Yat-sen University, Shenzhen 518107, China. [4]Qingdao NCS Testing and Protection Technology Co. Ltd., Qingdao 266071, China. [5]These authors contributed equally: Caiqi Yao, Xinru Wang. ✉email: zhangw286@mail.sysu.edu.cn

Mg^{2+} in seawater (Eq. (3)), thereby producing $Mg(OH)_2$.

$$O_2 + 2H_2O + 4e^- \rightarrow 4OH^- \tag{1}$$

$$2H_2O + 2e^- \rightarrow H_2 \uparrow + 2OH^- \tag{2}$$

$$Mg^{2+} + 2OH^- \rightarrow Mg(OH)_2 \downarrow \tag{3}$$

The increase in pH also shifts the equilibriums of an inorganic C reaction (Eq. (4)) and the $CaCO_3$ precipitation reaction (Eq. (5)) forward, resulting in $CaCO_3$ deposition.

$$OH^- + HCO_3^- \rightarrow H_2O + CO_3^{2-} \tag{4}$$

$$Ca^{2+} + CO_3^{2-} \rightarrow CaCO_3 \downarrow \tag{5}$$

$CaCO_3$ is the main protective component of the deposition layer, and its critical pH for deposition is 7.9[31].

In a seawater environment, the change in pH at the steel structure/seawater interface is the primary factor for the precipitation of Ca^{2+} and Mg^{2+}. Therefore, any factor, such as cathodic protection potential, cathodic protection current density, cathodic polarisation time and wetting state, liquid film thickness, and dissolved O_2 content, that can affect the pH of this interface will change the polarisation behaviour of the steel structure and deposition of Ca^{2+} and Mg^{2+}, thus influencing the protective performance of the Ca layer[23,32].

Marine tidal range is a complex environment with multiple phases and interfaces. The corrosion factors are non-uniformly distributed in this range due to different seawater immersion rates, surface liquid film thicknesses, and liquid film residence times at different heights. Clearly, although research on the effects of this environmental inhomogeneity on the formation of a Ca and Mg deposition layer and its protective performance is of important theoretical significance and application value, to date, no comprehensive studies have been conducted in this regard. Herein, the development of a Ca and Mg deposition layer in the tidal zone and its effects on the corrosion and protection of a base metal under cathodic protection were analysed by wire beam electrode (WBE) technique, electrochemical impedance spectroscopy (EIS), and scanning electron microscopy (SEM), energy-dispersive X-ray spectroscopy (EDS), and other techniques.

RESULTS AND DISCUSSION

Morphological characterisation by SEM and EDS

Figure 1 shows the electrode surface topography and magnified images of the local areas at 40 days of experiment. From the full immersion zone to the high-tide zone, a white deposited layer attached to the electrode surface was noticed; nevertheless, the degree of coverage of the deposited layer sequentially decreased. Except for the case of the full immersion zone, the higher the tidal zone area, the more serious the electrode surface corrosion.

The larger the R_{im}, the longer the immersion time and the longer the cathodic protection time. In the full immersion zone, R_{im} was 100%, and the electrode surface was covered with white Ca and Mg deposits (Fig. 1d). No rust spots were found on the surface of the electrode, indicating that the corrosion of the base metal was effectively controlled. With an increase in the tide level, for example, in the case of the 9th row of the mid-tide level (R_{im}-9: 62.5%), the colour of the Ca and Mg layer deposited on the metal surface gradually darkened, and yellow-brown rust spots were visible in the local area (Fig. 1c). In the case of the 14th row of the high-tide level (R_{im}-14: 20.8%), the corrosion spots were continuous and brownish (Fig. 1b).

The rusting products in the tidal zone are negatively correlated with R_{im}, that is, the larger the R_{im}, the higher the coverage of the deposited layer. Note that "defective areas" with partially peeled deposited layers were found on the electrode surface in the full immersion zone with different areas (Fig. 1a, d).

Current density and potential distribution of the WBE

Current density distributions of the electrode surface during typical stages of flood and ebb tides over a 40-day period are depicted in Fig. 2. Figures 3 and 4 show the average cathodic protection current densities and protection potentials with respect to time for a single row of five electrodes at different tide levels corresponding to them (results corresponding to days 4 and 7 are not shown).

On the 1st day, the current density was uniformly distributed on the electrode surface during the flood and ebb tides (Fig. 2a). With a decrease in the tide level, the submerged area reduced, and the average protection current density gradually increased from 58.9 $\mu A \cdot cm^{-2}$ at H1 to 113.9 $\mu A \cdot cm^{-2}$ at L (Fig. 3a). Simultaneously, the cathodic protection current density increased, cathodic polarisation enhanced, and the cathodic protection potential gradually shifted negatively from −0.99 (vs. SCE) to −1.00 V (vs. SCE) at L (Fig. 4a). The cathodic protection potential and current density changed in opposite directions during the flood tide (Figs. 3b and 4b), which were symmetrically distributed during the flood and ebb tides.

The potential interval of the submerged region during the flood and ebb tide stages was in the range from −0.96 to −1.03 V (vs. SCE) (Fig. 4a, b), which was in accordance with the international standard code recommending a protection potential interval of −0.78 to −1.03 V (vs. SCE)[26]. This implied that the electrodes at different tide levels were efficiently protected from corrosion. In the seawater environment, when the polarisation potential is ≥−0.95 V (vs. SCE), the cathodic reaction is mainly Eq. (1), that is, the reduction of dissolved O_2, which is controlled by diffusion[28,29]. Nevertheless, when the potential is ≤−1.10 V (vs. SCE), the cathodic reaction is primarily Eq. (2), namely, the reduction of H_2O, which is controlled by activation[28,33]. Thus, in the potential interval of −0.96 to −1.03 V (vs. SCE), these two cathodic reduction reactions (Eq. (1) and (2)) simultaneously occur on the electrode surface. Consequently, the pH at the base metal/seawater interface increases, thereby promoting the deposition of $Mg(OH)_2$ (Eq. (3)) and $CaCO_3$ (Eq. (5)) on the metal surface and reducing the current density required for cathodic protection[34,35]. Thus, the average protection current density at different tide levels decreased on day 4 (Fig. 2b); for instance, the average protection current densities at H1 and L decreased to 42.5 and 76.1 $\mu A \cdot cm^{-2}$, respectively, which indicated that protective Ca and Mg deposition layers started to form at all different tide levels[24,36,37].

The current monitoring results of the sacrificial anode on the 1st day at different tide levels showed that the total current generated by the sacrificial anode was 855.4 μA at H1 and only 670.5 μA at L. This suggests that the sacrificial anode can adjust the current output based on the demand for cathodic protection and has a certain self-regulation function.

On the 7th day, cathodic protection current densities at different tide levels again decreased to 32.7 and 54.2 $\mu A \cdot cm^{-2}$ at H1 and L, respectively, indicating an increase in the protection performance of the deposited layer. However, we also noticed that a stronger cathodic reaction zone appeared at H1 and H2, and the current density began to show a non-uniform distribution on the electrode surface (Fig. 2c).

On the 15th day, cathodic protection current densities at H1 and L decreased to 12.9 and 32.8 $\mu A \cdot cm^{-2}$, respectively. Moreover, the cathodic protection current densities during the flood and ebb tides were substantially different (Fig. 2d). During the flood tide stage, strong cathodic reaction zones were observed on the lower side of the dynamic waterline immediately adjacent to M2, MH, and H2, whereas this phenomenon was not
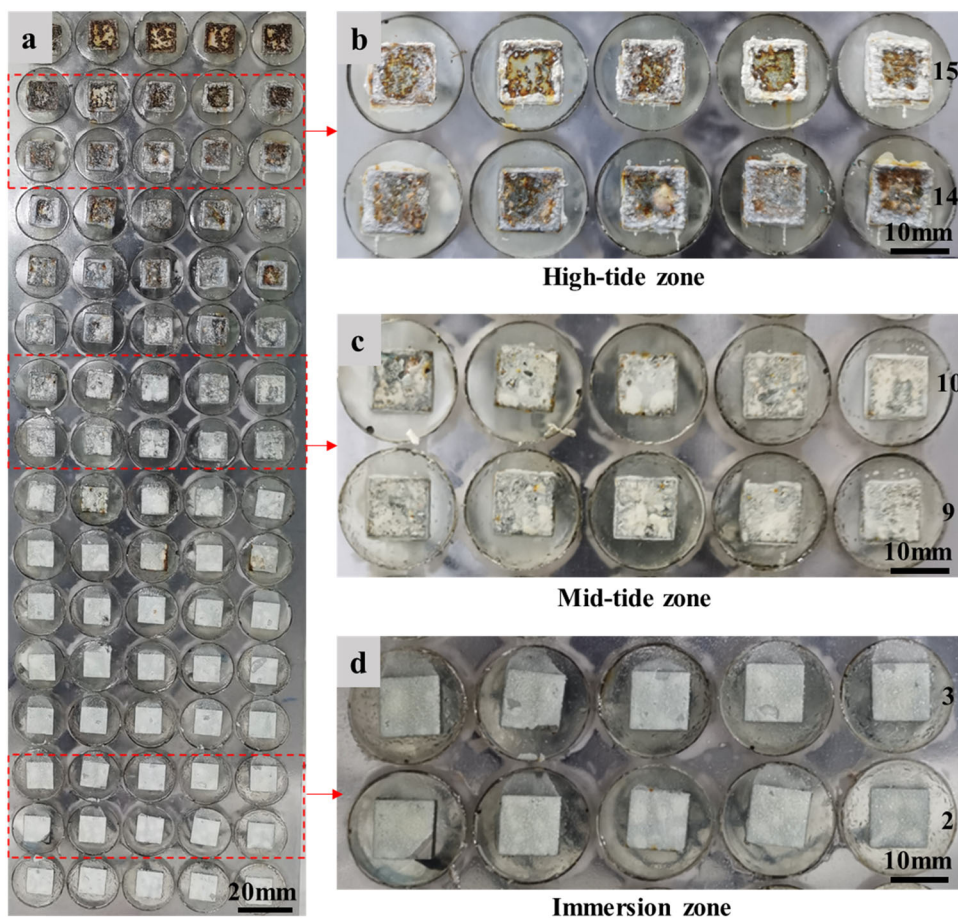
Fig. 1 Images of electrode surfaces. a Entire electrode surface. **b** Magnified images of the local areas: 14 and 15 rows. **c** 9 and 10 rows. **d** 2 and 3 rows.

noticed during the ebb tide stage. For example, the average current density of the electrode in the 13th row at HM was only 19.7 $\mu A \cdot cm^{-2}$, whereas that of the electrode in the 13th row at MH increased to 109.8 $\mu A \cdot cm^{-2}$ (Fig. 3c, d). Corresponding to the increase in the cathodic protection current density, the average cathodic protection potential gradually shifted positively from −1.06 (vs. SCE) to −0.80 V (vs. SCE) during the flood tide stage, and the potentials of some electrodes shifted to the unprotected range (Fig. 4d).

On the 23rd day, the unevenness of the cathodic protection current density distribution during the flood and ebb tide stages further increased (Fig. 2e), and the dynamic water-line area near all tide levels in the tidal zone during the flood tide stage showed a larger cathodic current area. Simultaneously, the cathodic protection current density slowly increased. Taking MH as an example, the average current density of the electrode in the 13th row reached 265.3 $\mu A \cdot cm^{-2}$ (Fig. 3f), which was approximately three times that on the 15th day. Furthermore, the cathodic protection potential was considerably different at different cathodic protection current densities. During the ebb tide stage, the average cathodic protection potential gradually shifted negatively from −0.95 V (vs. SCE) at H1 to −1.06 V (vs. SCE) at L (Fig. 4e). During the flood tide stage, the cathodic protection potential slowly shifted positively again with strong cathodic depolarisation in the dynamic water-line region (Fig. 4f). For instance, at MH, the cathodic protection potential gradually shifted positively to −0.78 to −0.72 V (vs. SCE), leaving the entire submerged zone in an underprotected state[26].

By the 40th day, the area of the high-speed cathodic reaction region during the upwelling phase was significantly reduced,

maintaining only two to three rows near the dynamic water-line (Fig. 2f). Nevertheless, the cathodic current density in this region increased again. For example, the average current density of the electrode in the 13th row at M2 increased to 331.1 $\mu A \cdot cm^{-2}$ (Fig. 3g). Simultaneously, the cathodic protection current density slowly increased and rapidly shifted positively, moving the cathodic protection potential at M2 to the unprotected range.

The stronger O_2 depolarisation near the dynamic water-line during the flood tide stage also gradually increased the demand of average cathodic protection current density. Taking the cases of M1 and M2 as examples, the cathodic protection current density decreased from 75–80 to 20–30 $\mu A \cdot cm^{-2}$ with the gradual coverage of the deposition layer on the metal surface during the initial 1–14 days. The cathodic protection current densities during the flood and ebb tide stages were similar and symmetrically distributed (Fig. 5). However, with the emergence of a stronger cathodic reaction zone near the dynamic water-line, the cathodic protection current density during the flood tide stage continuously increased to 70.3 $\mu A \cdot cm^{-2}$ at 40 days, whereas that during the ebb tide stage slowly decreased to 11.7 $\mu A \cdot cm^{-2}$. The decrease in the cathodic protection current density at M1 implies an increase in the protection performance of the calcareous deposits. The higher current density of the cathodic reaction in the dynamic water-line area after 14 days of the flood tide stage was attributed to the microstructure of the deposited layer and flood and ebb tide effect.

In summary, in the full immersion zone, the cathodic protection current density decreased from 113.9 $\mu A \cdot cm^{-2}$ during the initial stage to 11.0 $\mu A \cdot cm^{-2}$ on the 40th day, which was 1/10 of that during the initial stage. In contrast, the average cathodic
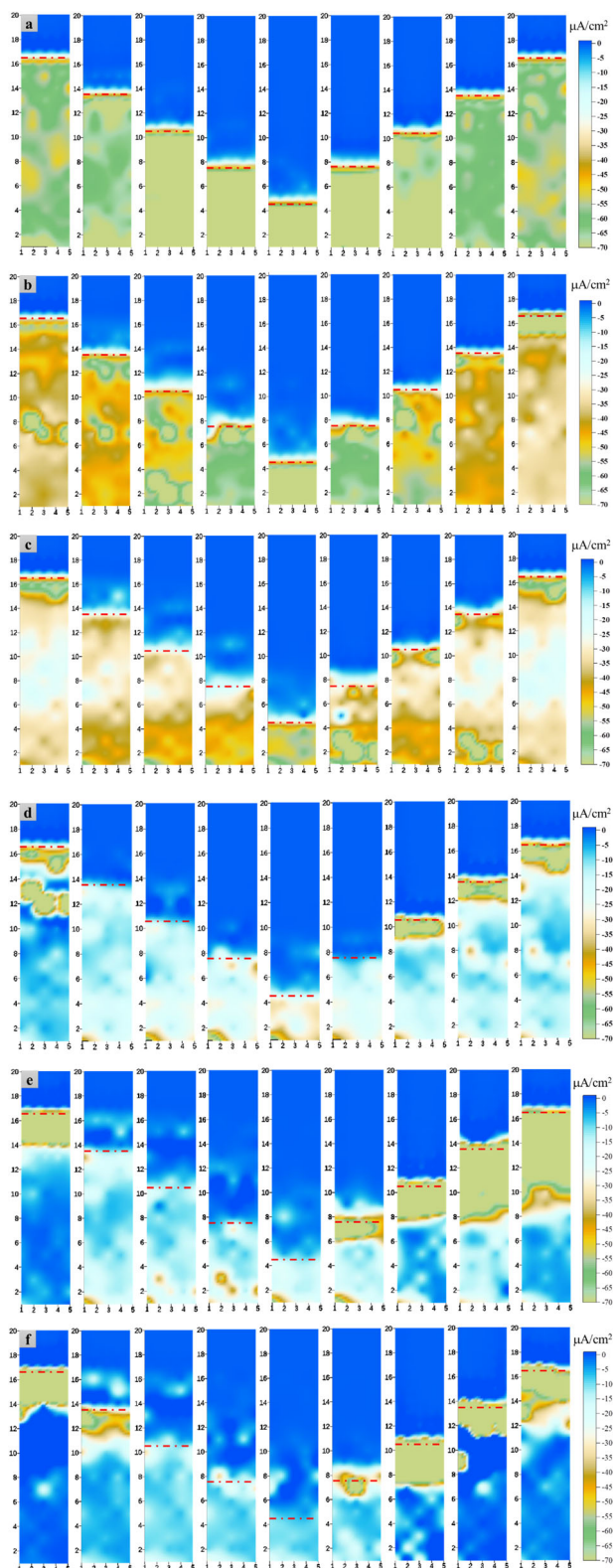
Fig. 2 Current density distributions. Figures **a**, **b**, **c**, **d**, **e**, and **f** represent the current density distributions on day 1, 4, 7, 15, 23, and 40 of experiment, respectively.

protection potential remained at −1.00 to −1.08 V (vs. SCE). In this potential range, both the reduction reactions in Eq. (1) and (2) occur on the electrode surface, and the H_2 gas produced by the reduction of water in Eq. (2) diffuses outward from the base metal

surface via the deposited layer, which can cause cracking or peeling of the deposited layer[21]. We believe that the local defect pits in the layer deposited on the surface of the electrode in the full immersion zone (Fig. 1) are owing to H_2 precipitation leading to the rupture of the deposited layer.

For instance, for the tidal zone, the current densities of the electrodes at M1 and M2 slowly decreased from 1 to 14 days and were symmetrically distributed on flood and ebb tide. Moreover, during 14−37 days, the cathodic protection potential slowly increased due to the strong cathodic O_2 reduction reaction in the dynamic water-line area at M2. Simultaneously, the cathodic protection potential gradually shifted to the unprotected range.

EIS

Figures 6, 7 and 8 depict the variation trends of impedance spectra with respect to time for 3-1# (the first electrode in row 3 in the full immersion zone), 9-1# (the first electrode in row 9 at mid-tide level), and 14-1# (the first electrode in row 14 at the high-tide level), respectively. The impedance spectrum of 3-1# exhibited a semicircular arc in the high-frequency region and a diffusion tale in the low-frequency region from 1 to 7 days (Fig. 6a). The cathodic protection current density of 3-1# gradually decreased during this time, which should be the stage of continuous generation of the deposition layer[28,38]. Nevertheless, owing to the low impedance of the deposited layer, the electrochemical processes associated with this layer are not reflected in the impedance spectrum. Therefore, the equivalent circuit shown in Fig. 9a was employed to fit the impedance spectral response during this period 38, where R_s is the solution resistance, Q_{dl} is the double-layer capacitance of the corrosion reaction at the solution/base metal interface, R_{ct} is the charge transfer resistance, and W is the cathodic finite-length Warburg impedance. From day 8 onwards, a small semicircular arc appeared in the high-frequency region of the Nyquist plot of impedance spectrum, and the diameter of this semicircular arc gradually increased with time (Fig. 6b). The appearance of this semicircular arc in the high-frequency region should be owing to the coverage of the metal surface by the deposited layer, and the radius of the impedance arc slowly increased, suggesting a gradual increase in the protective properties of the deposited layer[39]. We fitted the impedance spectral response during this time utilizing the equivalent circuit shown in Fig. 9b, where R_s is the solution resistance, $Q_{dl,f}$ is the bilayer capacitance of the deposited layer, R_f is the charge transfer resistance of the deposited layer, Q_{dl} is the bilayer capacitance of corrosion at the deposited layer/base metal interface, R_{ct} is the charge transfer resistance, and W is the cathode finite length Warburg impedance.

The Nyquist plot in the impedance spectrum acquired during 1–9 days of experiment also exhibited a semicircular arc with a diffusion tail (Fig. 7a). The emergence of a distinct semicircular arc in the high-frequency region was noticed in the impedance spectrum obtained on day 10, which demonstrated two semi-circular arcs and a semicircular arc with diffusion tails at low frequencies (Fig. 7c). The results of some studies have shown that the Mg-rich deposition layer (inner layer) and Ca-rich deposition layer (outer layer) exhibit two separate semicircular arcs in the high-frequency region of the impedance spectrum due to the different barrier properties of these layers[28]. Consequently, we used the equivalent circuit fit with three time constants shown in Fig. 9c and obtained a better fit (Fig. 7c), where $Q_{dl,fi}$ and $Q_{dl,fo}$ represent the capacitances of the inner and outer deposition layers, respectively, and R_{fi} and R_{fo} are the resistances of the inner and outer layers, respectively.

Initial impedance spectral response of 14-1# is consistent with those of 3-1# and 9-1# (Fig. 8). A small semicircular arc appeared in the high-frequency region of the impedance spectrum obtained
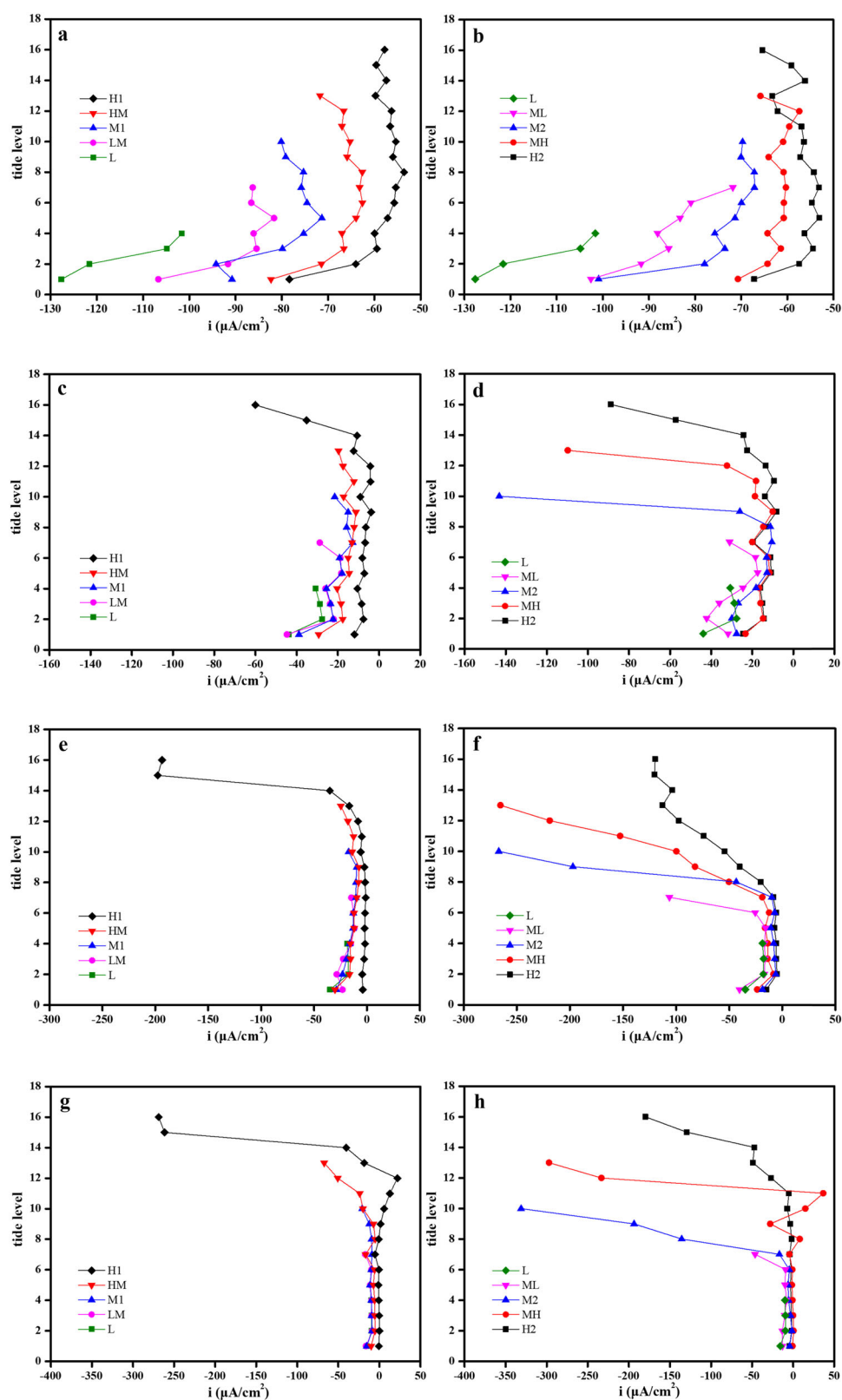
Fig. 3 Average current density distributions. Average current density distributions of a single row of five electrodes at different tide levels on **a**, **b** 1st, **c**, **d** 15th, **e**, **f** 23rd, and **g**, **h** 40th day of experiment.

on the 10th day. The semicircular arc in the high-frequency region and the semicircular arc with a diffusion tail in the low-frequency region were maintained until the end of the experiment. We used the same equivalent circuits as those employed in the case of 3-1#

(Fig. 9a, b) for impedance spectrum fitting and achieved suitable fits.

Figure 10 depicts the variation of the resistances of the Ca and Mg deposition layer with respect to time at different tide levels.
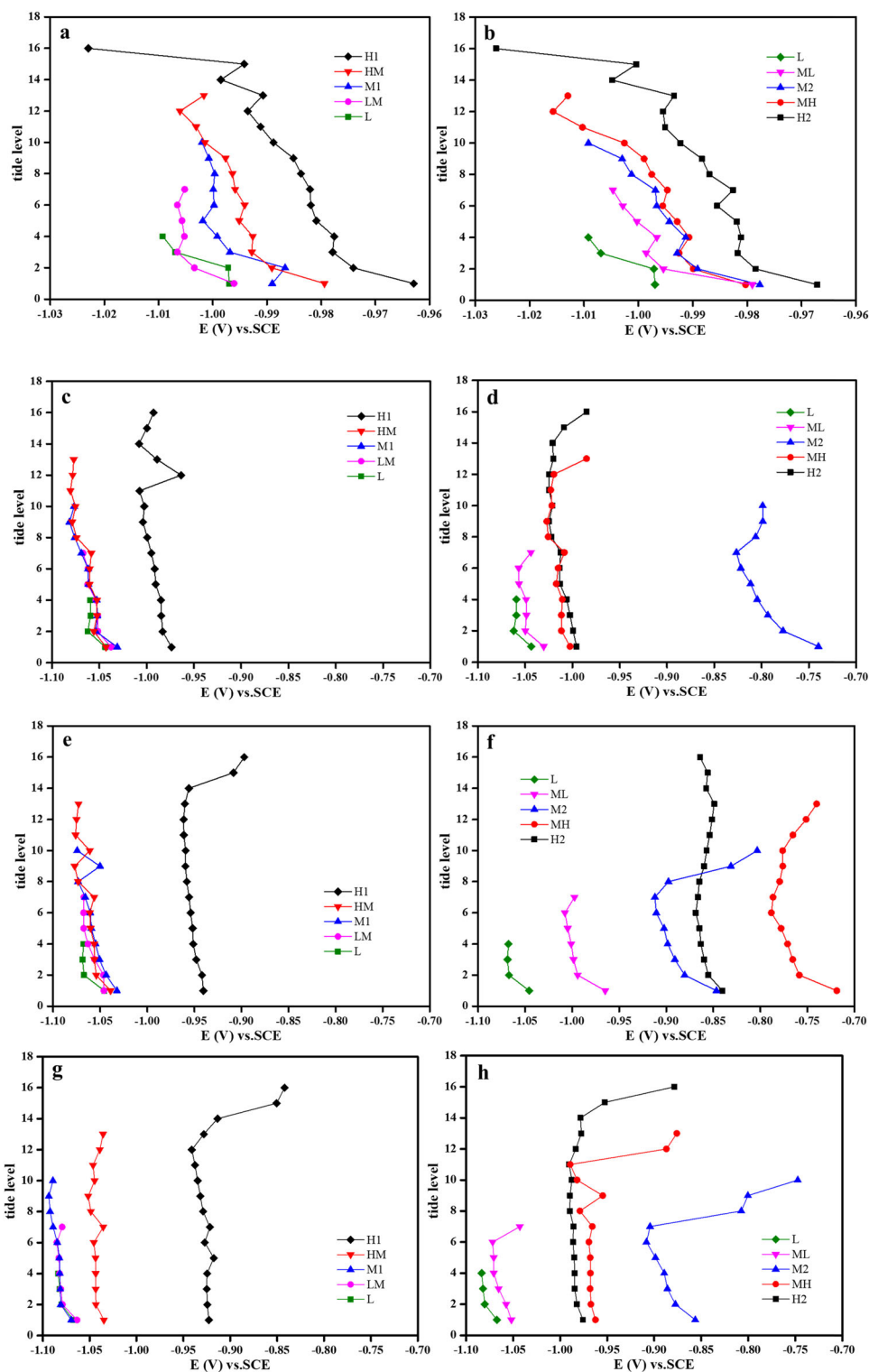
Fig. 4   Average potential distributions. Average potential distributions of a single row of five electrodes at different tide levels on **a**, **b** 1st, **c**, **d** 15th, **e**, **f** 23rd, and **g**, **h** 40th day of experiment.

For 3-1#, although the impedance arc associated with the deposited layer was detected in the high-frequency region of the impedance spectrum acquired on the 8th day, the initial growth of the deposited layer was slow and the impedance was still less than 50 Ω cm² at 15 days (Fig. 10a). The low initial impedance and slow growth of the deposited layer in the full immersion zone may be related to the precipitation of H_2 during

the water reduction reaction (Eq. (2)) occurring on the surface of this layer, resulting in the detachment of the localised deposited layer and difficulty in its effective attachment[40] (Fig. 1d). In contrast, for 9-1#, although the presence of the deposited layer slightly later than that in the case of 3-1# was detected in the impedance spectrum, it increased rapidly afterwards, and the sum of the inner and outer resistances increased to 353 Ω cm² by

37 days (Fig. 10b). The deposition layer in the case of 14-1# emerged at a similar time as that in the case of 9-1#; nevertheless, the impedance of this layer increased more slowly, reaching a maximum of 88 Ω cm^2 by 27 days, and then rapidly decreased to 55 Ω cm^2 by 35 days (Fig. 10c).
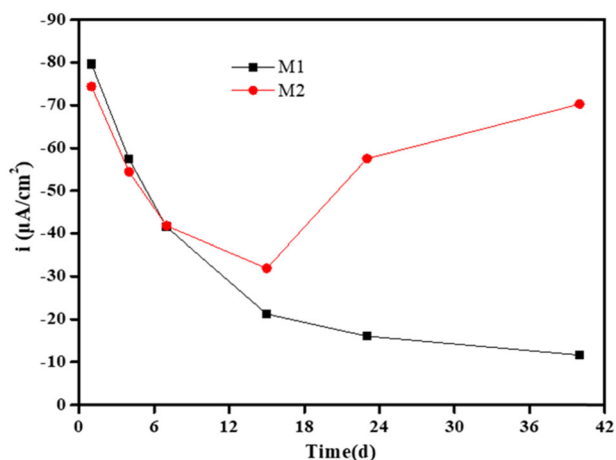

Fig. 5 Current trend at mid-tide level. Variation trend of average cathodic protection current density with time for M1 and M2.

Based on the abovementioned electrochemical impedance spectra at different tide levels and the variation of the resistance fitting results of the calcareous deposits with time, it can be concluded that the protection performance of the deposited layer is the best in the full immersion zone (although it more slowly increases at the beginning), followed by the mid-tide zone, and the deposited layer in the high-tide zone not only is slowly formed, but also has a weak protection performance. The variation trend of the impedance of the deposited layer is positively correlated with the tidal level and rust spots. That is, from the full immersion zone to the high-tide zone, with an increase in R_{im}, the protection time of the base metal becomes shorter, the growth rate of the deposited layer gradually decreases, the protection performance becomes inferior, and the corrosion degree of the base metal slowly increases.

Surface morphology and section element distribution

Figure 11 shows the SEM images of the surfaces and cross-sections of 3-1#, 9-1#, and 14-1# at the end of the test. In the case of 3-1#, fully developed cauliflower-shaped aragonite crystals ($CaCO_3$) with up to 150–200 μm diameters were observed on the surface of the deposited layer, and a large number of coral reef-like hydromagnesite crystals ($Mg(OH)_2$, lighter in colour) grew on the surfaces of the aragonite crystals or at the marginal joints (Fig. 11a). The deposited layers were approximately 250–300 μm
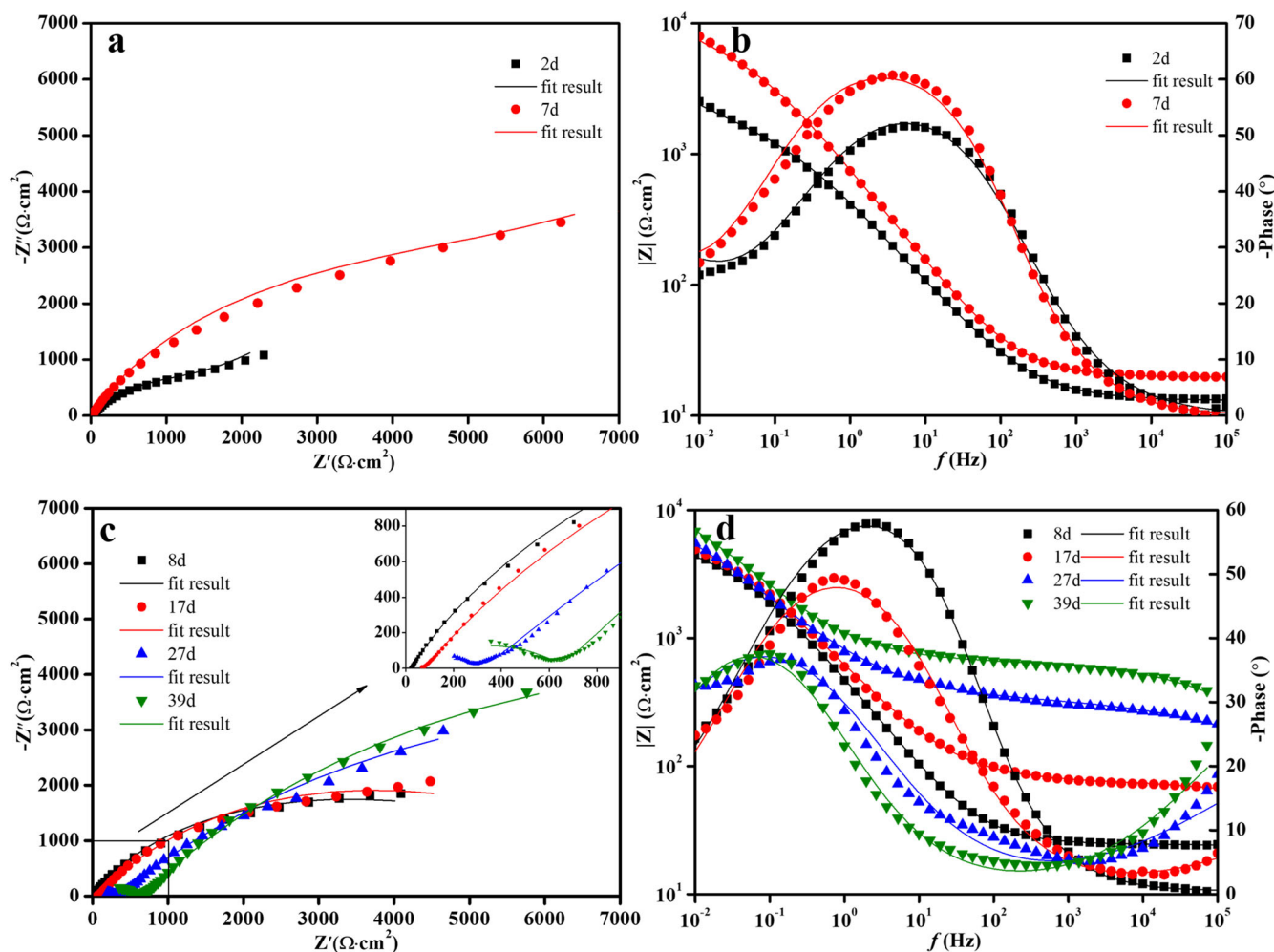

Fig. 6 EIS. Electrochemical impedance spectra of 3-1# (the first electrode in row 3 in the full immersion zone) with respect to time: **a, c** Nyquist plots and **b, d** Bode plots.
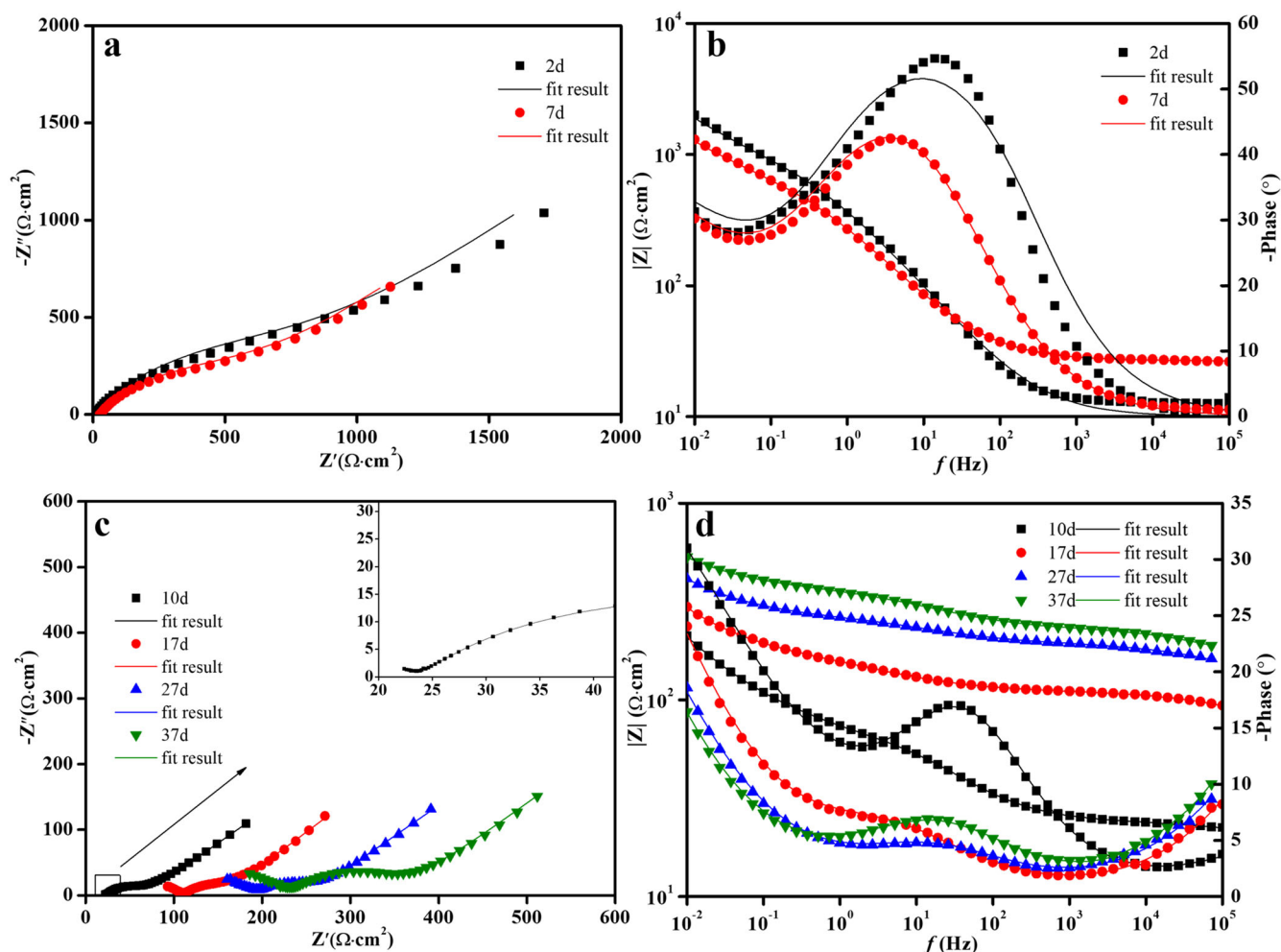
Fig. 7 EIS. Electrochemical impedance spectra of 9-1# (the first electrode in row 9 in the mid-tide zone) with respect to time: **a, c** Nyquist plots and **b, d** Bode plots.

thick and were tightly bound to the base metal with no significant delamination or gaps (Fig. 11b).

In the case of 9-1#, although the deposited layer surface was also covered with cauliflower-shaped aragonite crystals, these crystals were smaller in diameter, had larger cluster gaps, and were less well-developed than those in the case of 3-1# (Fig. 11c). Similarly, spherical hydromagnesite crystals grew on the surfaces of aragonite crystals and in the interstices. A gap was noticed between two white deposited layers with considerable delamination, and the deposited layer thickness was approximately 330–380 μm (Fig. 11d). The delamination of the deposited layers was confirmed by the presence of two time constants in the high-frequency region of the corresponding impedance spectrum.

In the case of 14-1#, the aragonite crystals were substantially less developed and were not spread over the entire surface in a coherent manner; instead, they were scattered on the surface of 14-1# in the form of small spheres (approximately 50–60 μm in diameter). Needle-shaped aragonite crystals were scattered among the spherical particles, which were underdeveloped. Moreover, considerable cracks were observed on the surface of the deposited layer (Fig. 11e). The deposited layer detached from the base metal, and 250–300 μm crevice was observed (Fig. 11f), increasing the height of the entire deposited layer to 600–700 μm.

According to the surface morphologies of the abovementioned three typical electrodes, it can be deduced that the degree of aragonite crystal development deteriorates from the full immersion zone to the mid-tide zone and the high-tide zone. Specifically,

small spherical aragonite crystals were scattered on the surface of 14-1# in the form of islands, with needle-like underdeveloped aragonite grains in the middle. The development of aragonite crystals is highly consistent with the tide position: the higher the tide level, the inferior the development of aragonite crystals and the smaller the sizes of these crystals. Although the high tide level in the tidal zone led to a large cathodic protection current density during the flood tide stage from day 7 onwards, a complete cover layer was not formed on the metal surface. The reason for this should be the short submergence time, which slows the growth and development of crystals.

SEM and EDS were used to analyse the distributions of elements in the local area of a section of the deposited layer (Fig. 12). The Mg-rich (Mg(OH)$_2$) inner layer is in contact with the base metal under full immersion conditions, and the Ca-rich (CaCO$_3$) outer layer, which is the most common calcareous deposits structure[28], is immediately above the inner layer, with Mg element running throughout the outer cross-section of the deposited layer (Fig. 12a). The production and mechanism of deposition of these layers have been systematically investigated previously[37,41,42] and therefore have not been described herein.

The deposition of Mg(OH)$_2$ within the crevices of CaCO$_3$ crystals has also been demonstrated[28]. This phenomenon suggests that during the growth of CaCO$_3$ crystals, the pH within the microporous channels in the crystal particles exceeds 9.5, which induces the deposition of Mg(OH)$_2$[25]. The reason for this is that although the Mg-rich Mg(OH)$_2$ layer is preferentially deposited on
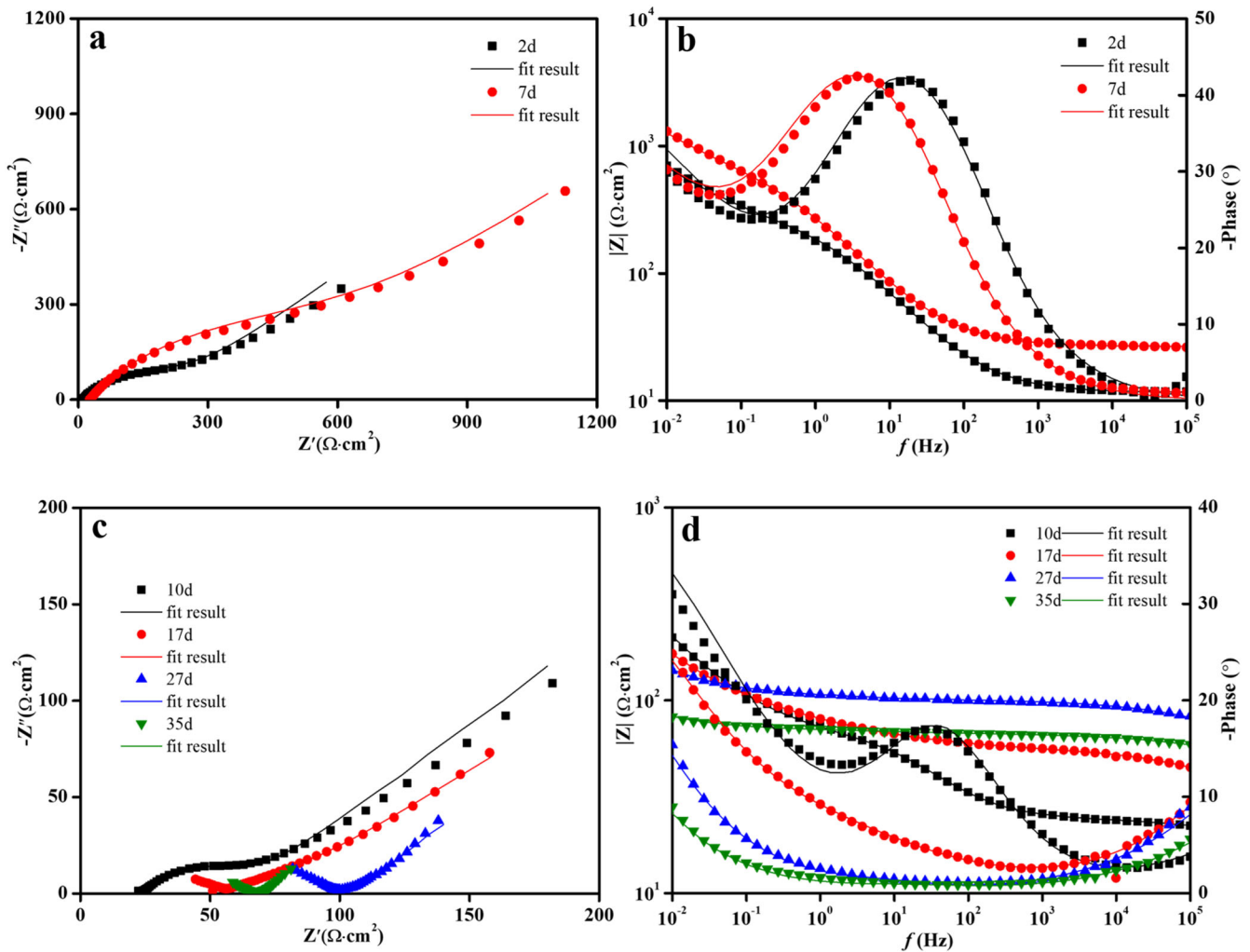
Fig. 8 EIS. Electrochemical impedance spectrum of 14-1# (the first electrode in row 14 in the high-tide zone) with respect to time: **a**, **c** Nyquist plots and **b**, **d** Bode plots.
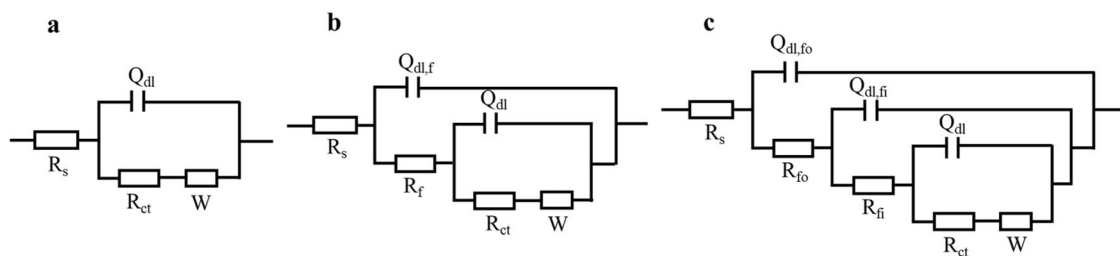

Fig. 9 Equivalent circuits. R_s is the solution resistance, $Q_{dl,f}$ is the bilayer capacitance of the deposited layer, R_f is the charge transfer resistance of the deposited layer, Q_{dl} is the bilayer capacitance of corrosion at the deposited layer/base metal interface, R_{ct} is the charge transfer resistance, and W is the cathode finite length Warburg impedance.

the electrode surface, because of the gel-like nature of $Mg(OH)_2$[40], it does not effectively prevent the cathodic reaction; nevertheless, it reduces the rate of the cathodic reaction and slightly decreases the cathodic protection current density. The reduction in the cathodic protection current density is more favourable to the precipitation of $CaCO_3$ than that of $Mg(OH)_2$[43]; thus, $CaCO_3$ with a stronger protective effect is deposited immediately above the $Mg(OH)_2$ layer. As the Ca-Mg deposition layer is an insulator, cathodic depolarisation (Eq. (1) or Eq. (2)) cannot be completed on the surface or inside the deposited layer and can only occur on

the surface of the base metal beneath the deposited layer. Therefore, the gaps or microporous channels between the $CaCO_3$ crystals preferably become channels for the diffusion of the depolarising agent to the metal surface. In contrast, the numerous OH^- generated by depolarisation will move along the gap channels and diffuse towards the deposition layer/seawater interface side. Thus, a channel with a decreasing pH gradient is formed along the micropores or gaps from the base metal surface to the seawater side. When the local pH within the deposited layer is higher than 9.5, $Mg(OH)_2$ is preferentially deposited;
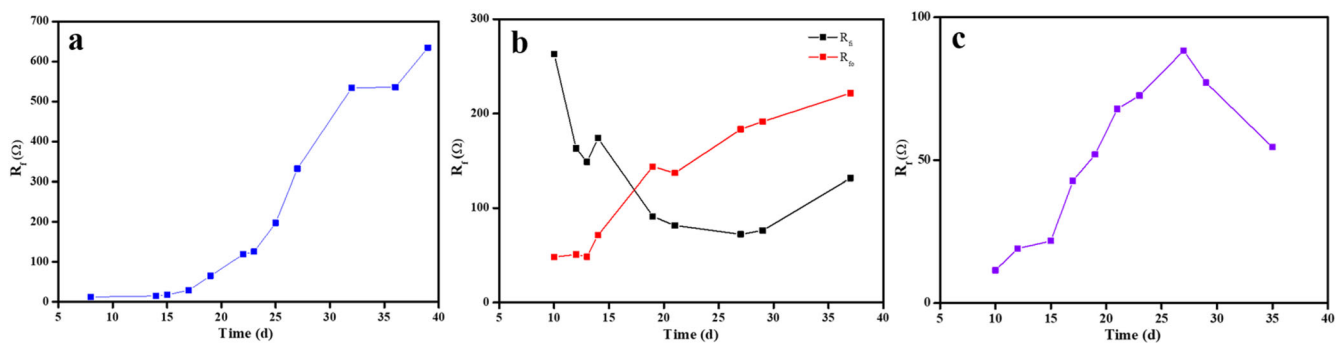
Fig. 10 Resistance of the deposited layer. Variation of the resistance of Ca-Mg deposition layer with time: **a** 3-1#, **b** 9-1#, and **c** 14-1#.
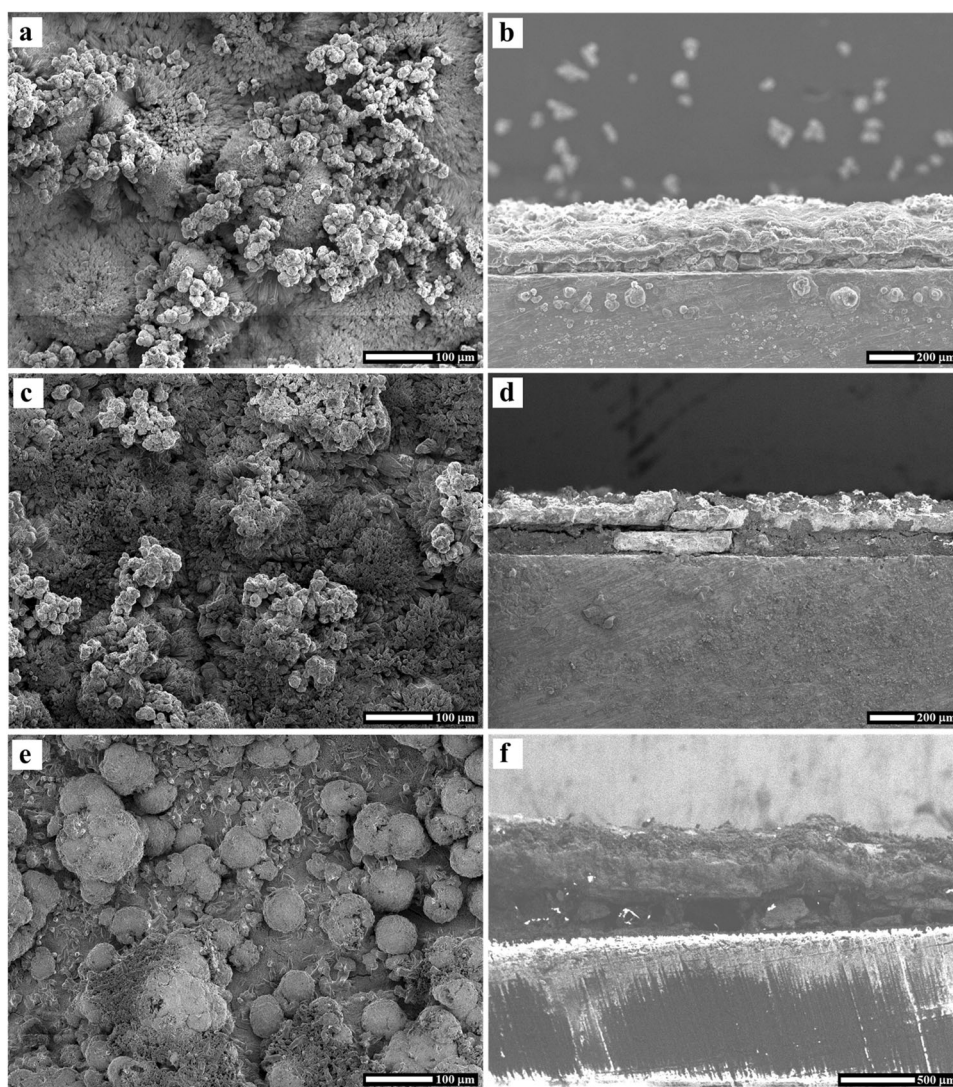

Fig. 11 SEM. Scanning electron microscopy images of the surfaces and cross-sections of electrodes at 40 days of experiment: **a**, **b** 3-1#, **c**, **d** 9-1#, and **e**, **f** 14-1#, respectively.

consequently, the growth of $Mg(OH)_2$ occurs within the developed pores and crevices of the calcareous deposits[25,28]. However, when the pH is between 8.5 and 9.5, $CaCO_3$ begins to precipitate. Thus, as these void channels are gradually blocked by the deposited layer, the barrier capacity and resistance of the deposited layer slowly increase (Fig. 10a).

SEM image of the mid-tide zone (Fig. 11d) reveals that the separated outer and inner layers are primarily composed of a Ca-rich layer, and the area between these two layers (circled by the red dashed line) is a Mg-rich layer (Fig. 12b). Note that this part of the deposited $Mg(OH)_2$ layer lay in a "tongue" shape between the $CaCO_3$ layers instead of lying flat on the electrode surface. The

phenomenon of two time constants in the high-frequency region of the impedance spectrum of the mid-tide zone should be attributed to the stratification of the deposited layer structure; nevertheless, we cannot yet confirm whether Q_{fi} and R_{fi} and Q_{fo} and R_{fo} correspond to the specific Ca-rich and Mg-rich layers based on the present experimental data only. However, the stratification of the deposited layers is certainly reflected in the high-frequency region of the impedance spectrum, which shows the typical characteristics of three time constants.

In the high-tide zone, we detected the detachment of the deposited layer from the base metal and did not notice the distribution of any elements associated with the corrosion of the base metal or the deposited layer in the overhanging gap shown in Fig. 11f. This part with a nearly 300 µm height is a gap left owing to the detachment of the deposited layer from the surface of the base metal. The Mg-rich layer is deposited immediately above the gap and runs through the Ca-rich layer above it, which is typical of the structure of the calcareous deposits[28].

In the mid-tide zone, particularly in the high-tide zone, spots of corrosion products were observed on the surface of the deposited layer (Fig. 1); nevertheless, only a small distribution of elemental Fe was detected in the cross-section EDS maps (Fig. 12b, c). Less corrosion products in the tidal zone implied that the corrosion of the base metal was mild, and cathodic protection and consequent generation of the Ca and Mg deposition layer still played certain protective roles.

The higher cathodic current zone near the dynamic waterline in the high-tide zone did not appear at the beginning; instead, it started to emerge on the 7th day, and its area gradually increased on the 15th day, after which it slowly enhanced with time. The average cathodic protection current density in the high-tide zone slowly decreased during the first 6 days of the test. For example, it was 58.9 µA·cm^{-2} on day 1, whereas it decreased to 42.5 µA·cm^{-2} on day 4 and was 32.7 µA·cm^{-2} on day 7 (Fig. 2). This indicated that at this time, although the capacitive arc representing the deposited layer was not detected in the high-frequency region of the impedance spectrum (Fig. 6a), the Ca and Mg deposition layer had started to form and provided some protection. Therefore, we believe that the appearance of the intense cathodic reaction zone near the dynamic waterline during the flood tide stage of the tidal zone is related to the formation of the deposited layer.

The impedance spectrum initially showed the impedance arc representing the deposition layer in the full immersion zone followed by the impedance arc denoting the deposition layer in the mid-tide zone and finally the impedance arc representing the deposition layer in the high-tide zone; furthermore, the quality (protection performance) of the deposited layer and the order of the appearance of its features in the impedance spectrum were consistent; the deposition layer in the full immersion zone was the best followed by that in the mid-tide zone, whereas the deposition layer in the high-tide zone was inferior.

The thickness of the layer deposited on the surface of 14-1# was approximately 300–400 µm (Fig. 11c), which was significantly higher than that for 3-1# (250–300 µm) (Fig. 11a). The immersion rate of 14-1# was only 20.8%, that is, the time of cathodic reaction on its surface to generate the calcareous deposits was only 1/5 of that for 3-1#, and the thickness of the deposition layer was lower than that in the case of 3-1#. Based on the low impedance of 14-1# (Fig. 10), slow development of CaCO$_3$ crystals on 14-1# (small particle sizes, Fig. 12b), and the presence of cracks (Fig. 12c) on the layer deposited on 14-1#, we believe that although the layer deposited on 14-1# is thick, its internal voids are high and the density is inferior than those in the cases of 3-1# and 9-1#.

Higher porosity and cracks inside the deposited layer provide convenient channels for the rapid diffusion of dissolved O$_2$ to the surface of the base metal, which offers favourable physical conditions to the high tide level to become an intense cathodic reaction zone. Contrary to the 3-1# and 9-1# deposition layers with appropriate protection performances (high impedance) and low porosities, the sparse deposition layer structure in the case of 14-1# was more inclined to form a rapid reaction zone for the reduction of dissolved O$_2$.

A higher cathodic reaction zone occurs during the flood tide stage rather than during the ebb tide stage, a phenomenon that may be related to not only the high content of dissolved O$_2$ near the dynamic waterline, but also the dry-wet cycling in the tidal zone[3,44]. These different processes caused by the immersion (water-absorbing expansion) and drying (water-losing contraction) of the deposited layer induced by the flood and ebb tides might be the reason for the different current densities of these electrodes. During the ebb tide stage, seawater gradually escapes out of the interior of the microporous channels of the deposited layer as the enters the electrode slowly dry state from submersion. The thinning of the liquid film in the internal pores also accelerates the reduction rate of dissolved O$_2$[28], which in turn creates a higher cathodic reaction area. However, during liquid film thinning, the liquid film resistance on the electrode surface gradually increases[1], and because of the two interactions, the falling tide stage does not exhibit a strong cathodic reaction zone. While during the flood tide stage, the low R_{im} of high tide level, in the longer drying process, because the deposited layer its main components of Mg(OH)$_2$ and CaCO$_3$ and the shrinkage ratio between the base metal is different[3], resulting in the separation between different components inside the deposited layer and generate internal stress makes the deposited layer rupture, forming the deposited layer overhang under the high tide level (Fig. 11f). When the deposited layer enters the liquid phase state, the micropores, crevices, and cracks inside the deposited layer entrap and store a large amount of O$_2$-rich aqueous solution from the dynamic waterline area under the effect of capillary. Consequently, an intense cathodic current zone of O$_2$ reduction reaction is generated near the dynamic waterline[5]. In addition to the high concentration of dissolved O$_2$ in the dynamic waterline zone, the consumed dissolved O$_2$ can be easily replenished; therefore, the cathodic reaction current can be sustained for a longer period of time[29]. Compared to that in the mid-tide zone, the deposited layer in the high-tide zone is less dense, less protective, and has high porosity; thus, a stronger cathodic reaction zone is developed (Fig. 2).

Because of dry-wet cycling, the deposited layer repeatedly undergoes water-absorbing expansion and water-losing contraction, and the porosity of the deposited layer in the mid-tide zone also starts to increase. Owing to the high-intensity cathodic reaction, the local pH in the inner hollow channel of the deposited layer rapidly increases[45], and a large amount of Mg(OH)$_2$ is extensively deposited to form a "tongue-like" Mg(OH)$_2$ layer interspersed between the CaCO$_3$ layers (Fig. 12b). Nevertheless, compared to the cases of 3-1# and 9-1#, a large amount of Mg(OH)$_2$ precipitates were not detected on the surface of 14-1#; this might be owing to the short submersion time of 14-1# and inferior quality of the formed CaCO$_3$ layer; thus, there was not enough space for Mg(OH)$_2$ attachment; in contrast, it was also possible that because of the high porosity of the deposition layer at the high-tide level, the OH$^-$ formed in a short period of time rapidly diffused into the solution and maked the growth rate of sedimentation of Ca and Mg compounds reduced. In summary, the following conclusions can be drawn.

1. From the full immersion zone to the high tide zone, with an increase in the tide level and a decrease in R_{im}, the development of aragonite CaCO$_3$ crystals in the deposited layer gradually decreased. At the same time, the deposited layer in the tidal zone of difference appears to be

delaminated or even detached from the surface of the substrate due to the dry-wet cycling. As a result, the protective properties of the deposited layer gradually weakened.

2. In the full immersion zone, with the gradual formation of the deposited layer, the protection performance was enhanced. Meanwhile, the corrosion of the base metal was effectively controlled.

3. At the beginning of the experiment, the cathodic protection current density gradually decreased with the formation of the calcareous deposits in the mid-tide zone. Simultaneously, the cathodic protection potential rapidly and positively shifted, leaving the metal in some of the tide levels in unprotected states.

4. During the flood tide stage, the high-speed O_2 reduction reaction near the dynamic water line is much higher than that in the immersion zone. This high-speed cathodic reaction current density accelerated the loss of the sacrificial anode in the immersion zone and the corrosion of the base metal in the adjacent area. This phenomenon should be fully considered in the design of tidal zone protection systems.
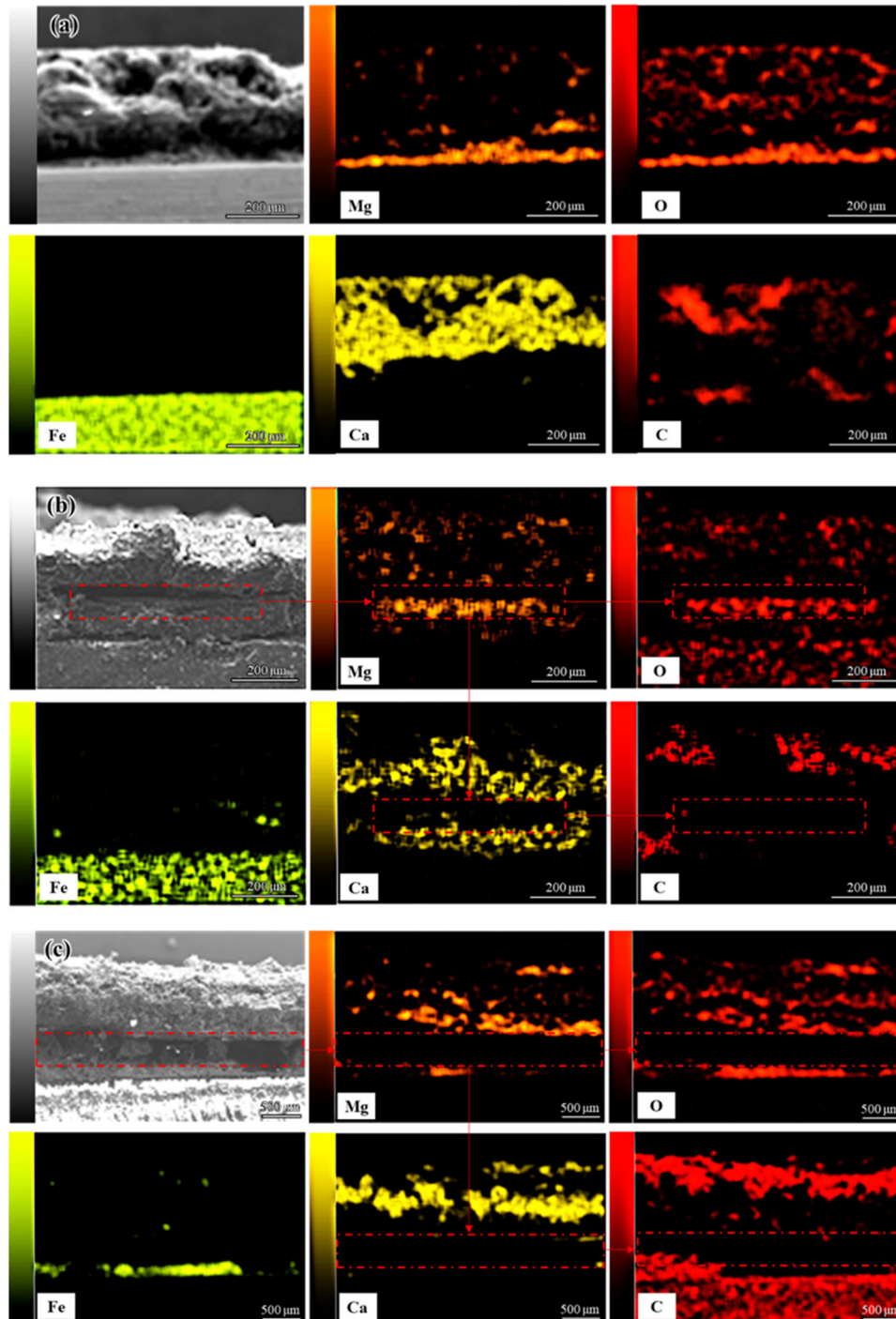

Fig. 12   SEM and EDS. Scanning electron microscopy images and energy dispersive X-ray spectroscopy maps of the deposited layer interface at different tide levels: **a** full immersion zone, **b** mid-tide zone, and **c** high-tide zone.

METHODS

WBE fabrication

The test metal was Q235 steel, and the exposed area of a single electrode was 10×10 mm^2 (namely, 1 cm^2). The single electrode was sealed as a φ 20 mm disc electrode with epoxy resin. Herein, 80 disc electrodes were embedded in a polyvinyl chloride template in a 16×5 array, with a distance of 10 mm between the upper and lower electrodes and the left and right electrodes, and the size of the entire array electrode was 320 mm× 100 mm (Fig. 13). The electrodes were separately arranged from bottom to top in 16 rows and from left to right in 5 columns. After sanding the surface of the specimen with 320#, 600#, and 1000# water-abrasive sandpaper, the specimen was rinsed and sequentially blown dry with acetone and ethanol.

The sacrificial anode used for cathodic protection in the test was the A13 Al anode recommended by the National Standard of Aluminium-Zinc-Indium Alloy Sacrificial Anode[46], and the composition of this anode is provided in Table 1. The sacrificial anode was cut into a φ10 × 50 mm^2 cylinder. The top of the cylinder was drilled and connected to a Cu wire. Electrochemical performance of the anode was investigated according to DNV-RP-B401 (2017) Appendix B[26] at an open circuit potential of −1.187 to 1.197 V (vs. SCE) and a working potential of −1.095 to 1.096 V (vs. SCE)[47]. Other electrochemical properties of the anode also met the

standard requirements. The cylindrical sacrificial anode was placed at the bottom of the WBE and connected to the WBE via a Cu wire (Fig. 13).

Tidal zone simulation device

The self-built tidal zone simulation device comprised a seawater tank and a ball screw linear module (including a linear slide table, numerical control servo/stepper motor, and controller) (Fig. 14). The simulation of flood and ebb tides in the tidal zone was achieved by a reciprocal cycle of upward and downward movement of the linear slide controlled by stepper motors.

The experiment was carried out indoors at an average room temperature of 24 °C and the experiment period was 40 days. In this experiment, the semi-diurnal tide was simulated. The array electrode moved at the speed of 40 mm·h^{-1}, and it took 6 hours to move from the low-tide line to the high-tide line. There were two high tides and two low tides every day. The low-tide line in the simulated tidal zone was in the middle of the electrode in the rows 4 and 5, the mid-tide line was in the middle of the electrode in the rows 10 and 11, and the high-tide line flooded over the electrode in the row 16. Rows 1–4 were the full immersion zone, and rows 5–16 were the tidal zone, among which the rows 5–8, 9–12, and 13–16 were the low-tide, mid-tide, and high-tide zones. Experimental seawater was surface seawater which obtained from Dalang Bay, Jiangmen, Guangdong Province. The seawater was settled for a month to separate the solid and liquid. The main components of seawater are shown in Table 2. The conductivity is 42.0 S · m^{-1}, and the concentration of dissolved oxygen measured by the dissolved oxygen tester (JPBJ-610L) is 6.54 mg·L^{-1}. 28 L seawater was injected into an electrolytic cell (size: 300 mm × 200 mm × 500 mm, Fig. 14) and replaced every 20 days during the experiment.

The immersion time: total time (the sum of immersion and drying times) ratio in one flood-ebb cycle (12 h) is called the immersion rate (R_{im}). For example, as row 1 was always immersed, its R_{im}-1 (R_{im} of the first row) was 100%. In contrast, R_{im}-16 (R_{im} of the 16th row) was only 4.2%.

WBE technique

The WBE experimental device is composed of NI PXI-2535, -4071, -1033, -4022 and other modular instruments[8,48]. The measurement and control software was customised using LabVIEW 8.5. The

Table 1. Composition of the Al-Zn-In-Si sacrificial anode A13.

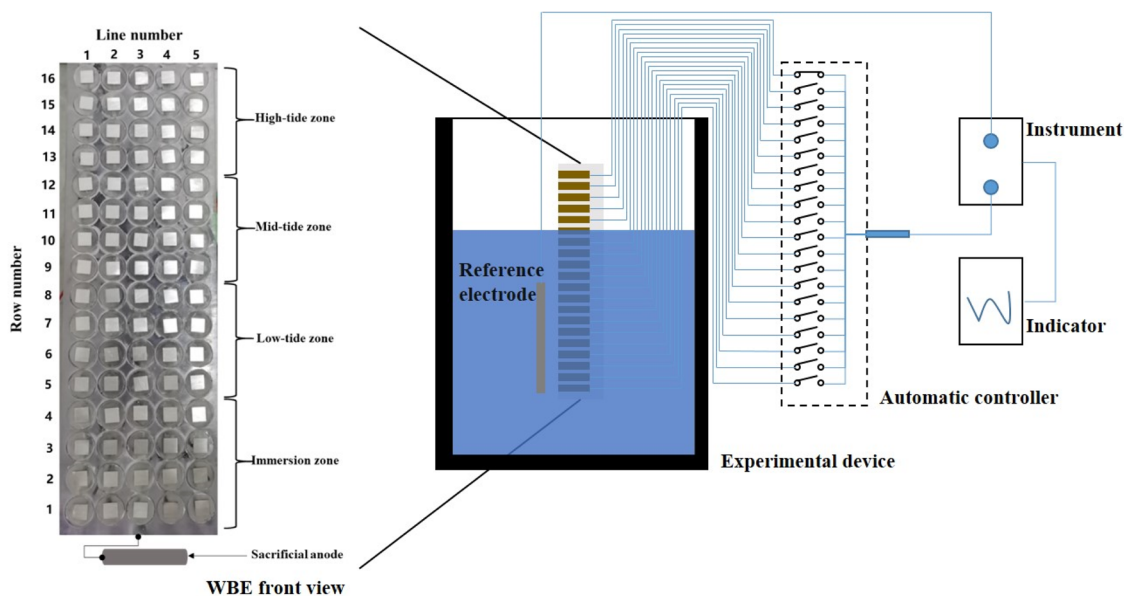| Chemical composition	Experimental quality fraction (%)	Standard quality fraction (%)
Al	94.500	92.555–94.115
Zn	5.310	5.500–7.000
In	0.027	0.025–0.035
Si	0.087	<0.100
Fe	0.047	<0.150
Ca	0.011	<0.100
Other	0.019	<1.500

Fig. 13 WBE. The diagram of the wire beam electrode test.

sacrificial anode was used as one of the electrodes. During the measurement of the local current, one electrode was disconnected and the other 80 electrodes were short-connected to each other to evaluate the current between this electrode and 80 coupling electrodes. The abovementioned process was automatically controlled by LabVIEW, and the data were plotted using Surfer 8.0.

Distributions of current density on the electrode surface at different tide levels were measured by the WBE experimental facility. Starting from the high-tide line position, a set of data was acquired for every three lines of movement, that is, the water line was collected using the WBE when it was located at the high-tide line (H1), mid high-tide line (HM), mid-tide line (M1), mid-low tide line (ML), low-tide line (L) in the ebb tide process, mid low-tide line (LM), mid-tide line (M2), mid high-tide line (MH), and high-tide line (H2) during flood tide. A total of nine current and potential distributions were evaluated in one flood-ebb cycle.

EIS

A Gamry interface 1010E electrochemical workstation was employed to obtain the electrochemical impedance spectrum. A WBE, a SCE, and a platinum electrode were used as the working, reference, and auxiliary electrodes, respectively. The scanning frequency range was 10^5–10^{-2} Hz, the amplitude of the alternate current excitation signal was 10 mV, and a representative single electrode was separately utilized for testing in the full immersion, mid-tide, and high-tide zones.

Scanning electron microscopy (SEM) and energy-dispersive X-ray spectroscopy (EDS)

At the end of the experiment, electrodes were separately acquired from the full immersion, mid-tide, and high-tide zones, and SEM (JSM-IT200A) and EDS were used to characterise the microstructure and elemental distribution of the Ca and Mg layer deposited on the surface of Q235 steel.

DATA AVAILABILITY

The date that support the findings of this study are available from the corresponding author upon reasonable request.

Table 2. Chemical composition of the seawater.

Chemical composition	c (g·L^{-1})	Chemical composition	c (g·L^{-1})
Na^+	7.4104	Cl^-	16.2263
Mg^{2+}	0.9787	SO_4^{2-}	2.6460
Ca^{2+}	0.3558	HCO_3^-	0.1709
K^+	0.5298	Br^-	/
Sr^{2+}	0.0039	F^-	/
Ba^{2+}	/		

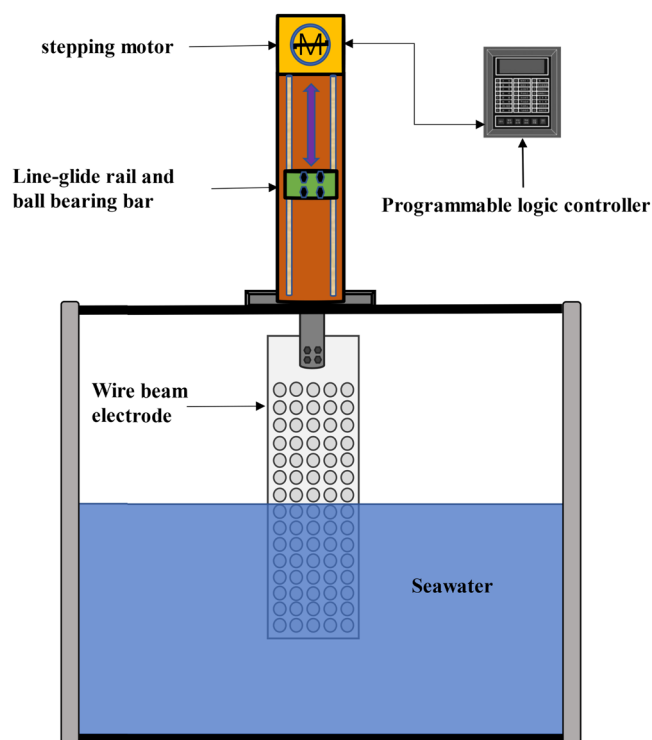/ represents a concentration less than 10^{-4} g·L^{-1}.

Fig. 14 Experimental device. Schematic of the tidal zone simulation device.

REFERENCES

1. Mu, X., Wei, J., Dong, J. & Ke, W. The effect of scarificial anode on corrosion protecion of Q235B steel in simulated tidal zone. *Acta Metall Sin-Engl* **50**, 1294–1304 (2014).
2. Hou, B. & Zhang, J. Corrosion behavior of steel in the tidal difference and full immersion zones. *Mar. Sci.* **4**, 16–19 (1980).
3. Mu, X., Wei, J., Dong, J. & Ke, W. In Situ Corrosion Monitoring of Mild Steel in a Simulated Tidal Zone without Marine Fouling Attachment by Electrochemical Impedance Spectroscopy. *J Mater Sci Technol* **30**, 1043–1050 (2014).
4. Hou, B., Yang, X. & Jia, S. Practice of Corrosion Protection and Multi-layer Covering Technology for Steel Structure in Splash Zone. *China Harbour Engineering* **179**, 70–72 (2012).
5. Chen, Y., Wang, W., Wang, J., Wang, Q. & Cai, G. Evaluation of Water-line Area Corrosion for Q235 Steel by WBE Technique. *J. Chin. Soc. Corros. Prot.* **34**, 451–458 (2014).
6. Chen, Z. et al. Research on the Metal Corrosion Process in the Sea Mud/Seawater/Atmosphere Interface Zone. *Coatings.* **10**, 70–72 (2020).
7. Ding, J. et al. Evaluation of Water-line Zone Corrosion of an Electrode with Coating in NaCl Solution by WBE Technique-I. *J. Chin. Soc. Corros. Prot.* **36**, 463–470 (2016).
8. Xia, W. et al. Comparison of cathodic protection processes of 40% zinc-rich coatings under immersion and atmospheric conditions: Protection for defective areas. *Electrochim. Acta.* **385**, 138450 (2021).
9. Deflorian, F. & Rossi, S. An EIS study of ion diffusion through organic coatings. *Electrochim. Acta.* **51**, 1736–1744 (2006).
10. Tan, Y. J., Bailey, S. & Kinsella, B. Mapping non-uniform corrosion using the wire beam electrode method. *III. Water-line corrosion. Corros. Sci.* **43**, 1931–1937 (2001).
11. Schumacher, M. Seawater corrosion handbook. Noyes Data Corp, https://www.osti.gov/biblio/6203524 (1979).
12. Stratmann, M., Streckel, H., Kim, K. T. & Crockett, S. On the atmospheric corrosion of metals which are covered with thin electrolyte layers-iii. the measurement of polarisation curves on metal surfaces which are covered by thin electrolyte layers. *Corros. Sci.* **30**, 715–734 (1990).
13. Mansfeld, F. & Tsai, S. Laboratory studies of atmospheric corrosion—I. Weight loss and electrochemical measurements. *Corros. Sci.* **20**, 853–872 (1980).
14. Nazarov, A. P. & Thierry, D. Scanning Kelvin probe study of metal/polymer interfaces. *Electrochim. Acta.* **49**, 2955–2964 (2004).
15. Mu, X., Wei, J., Dong, J. & Ke, W. Electrochemical Study on Corrosion Behaviors of Mild Steel in a Simulated Tidal Zone. *Acta Metall. Sin.* **48**, 420–426 (2013).
16. Park, J. H., Lee, G. D., Ooshige, H., Nishikata, A. & Tsuru, T. Monitoring of water uptake in organic coatings under cyclic wet-dry condition. *Corros. Sci.* **45**, 1881–1894 (2003).
17. Dai, Y. Design research and construction methods of corrosion protection for tidal zone and splash zone of foreign Harbor and offshore steel structures. *Waterway Harbor.* **1**, 33–53 (1981).

The labels on Fig. 14: stepping motor, Line-glide rail and ball bearing bar, Programmable logic controller, Wire beam electrode, Seawater.

18. Song, J., Lan, Z., Wang, Z. & Ji, J. Calcareous deposit formed under cathodic protection in the presence of natural marine sediments: A 12 month experiment. *Corros. Sci.* **31**, 265–267 (2010).

19. Solis, J. L., Genesca, J. In *Effect Of Calcareous Deposit Formation On Galvanic Anode Cathodic Protection Of Steel In Seawater*. 09520 (NACE Corrosion, 2009).

20. Wolfson, S. L. & Hartt, W. H. An Initial Investigation of Calcareous Deposits upon Cathodic Steel Surfaces in Sea Water. *Corrosion.* **37**, 70–76 (1981).

21. Carré, C. et al. Electrochemical calcareous deposition in seawater. A review. *Environ. Chem. Lett.* **18**, 1193–1208 (2020).

22. Rousseau, C., Baraud, F., Leleyter, L., Jeannin, M. & Gil, O. Calcareous deposit formed under cathodic protection in the presence of natural marine sediments: A 12 month experiment. *Corros. Sci.* **52**, 2206–2218 (2010).

23. Chen, S. & Hartt, W. H. Deepwater Cathodic Protection: Part 1—Laboratory Simulation Experiments. *Corrosion.* **58**, 38–48 (2012).

24. Barchiche, C. et al. Characterization of calcareous deposits in artificial seawater by impedance techniques. *Electrochim. Acta.* **48**, 1645–1654 (2003).

25. Mantel, K. E., Hartt, W. H. & Chen, T. Y. Substrate, Surface Finish, and Flow Rate Influences on Calcareous Deposit Structure. *Corrosion.* **48**, 489–500 (1992).

26. Veritas, D. N. Cathodic Protection Design. Veritas Recommended Practice Rpb. https://www.academia.edu/download/62072527/DNV-RP-B40120200211-18257-1ehcew1.pdf (1986).

27. Hartt, W. H. 2012 Frank Newman Speller Award: Cathodic Protection of Offshore Structures—History and Current Status. *Corrosion* **68**, 1063–1075 (2012).

28. Yang, Y., Scantlebury, J. & Koroleva, E. A Study of Calcareous Deposits on Cathodically Protected Mild Steel in Artificial Seawater. *Metals.* **5**, 439–456 (2015).

29. Evans, V. R. The corrosion and oxidation of metals (Second Supplementary Volume). https://trid.trb.org/view/61856 (1976).

30. Karoui, H. et al. Electrochemical scaling of stainless steel in artificial seawater: Role of experimental conditions on $CaCO_3$ and $Mg(OH)_2$ formation. *Desalination.* **311**, 234–240 (2013).

31. Akamine, K. & Kashiki, I. Corrosion Protection of Steel by Calcareous Electrodeposition in Seawater (Part 1) Mechanism of Electrodeposition. *Zairyo-to-Kankyo* **51**, 496–501 (2002).

32. Chen, S., Hartt, W. & Wolfson, S. Deep Water Cathodic Protection: Part 2-Field Deployment Results. *Corrosion.* **59**, 721–732 (2003).

33. Ashworth, V. & Booker, C. J. Cathodic protection: Theory and practice. https://www.osti.gov/biblio/6810893 (1986).

34. Zakowski, K., Szocinski, M. & Narozny, M. Study of the formation of calcareous deposits on cathodically protected steel in Baltic sea water. *Anti-Corros. Methods Mater* **60**, 95–99 (2013).

35. Ou, K. C. & Wu, J. K. Effect of calcareous deposits formation on the hydrogen absorption of steel. *Mater. Chem. Phys.* **48**, 52–55 (1997).

36. Humble, R. A. Cathodic Protection of Steel in Sea Water With Magnesium Anodes. *Corrosion.* **4**, 358–370 (1948).

37. Yan, J. F. Mathematical Modeling of the Formation of Calcareous Deposits on Cathodically Protected Steel in Seawater. *J. Electrochem. Soc.* **140**, 733–741 (1993).

38. Li, C. J. & Du, M. The growth mechanism of calcareous deposits under various hydrostatic pressures during the cathodic protection of carbon steel in seawater. *RSC Adv* **7**, 28819–28825 (2017).

39. Deslouis, C., Festy, D., Gil, O., Rius, G. & Tribollet, B. Characterization of calcareous deposits in artificial sea water by impedance techniques-I. Deposit of $CaCO_3$ without $Mg(OH)_2$. *Electrochim. Acta.* **43**, 1891–1901 (1998).

40. Barchiche, C., Deslouis, C., Gil, O., Refait, P. & Tribollet, B. Characterisation of calcareous deposits by electrochemical methods: role of sulphates, calcium concentration and temperature. *Electrochim. Acta.* **49**, 2833–2839 (2004).

41. Neville, A. & Morizot, A. P. Calcareous scales formed by cathodic protection—an assessment of characteristics and kinetics. *J. Cryst. Growth* **243**, 490–502 (2002).

42. Li, C., Du, M., Qiu, J., Zhang, J. & Gao, C. Influence of Temperature on the Protectiveness and Morphological Characteristics of Calcareous Deposits Polarized by Galvanostatic Mode. *Acta Metall Sin-Engl* **27**, 131–139 (2014).

43. Xing, Y. et al. Effect of surface calcareous deposits on hydrogen uptake of X80 steel under strong cathodic current. *Int. J. Hydrog.* **46**, 4555–4566 (2021).

44. Refait, P., Jeannin, M., Sabot, R., Antony, H. & Pineau, S. Corrosion and cathodic protection of carbon steel in the tidal zone: Products, mechanisms and kinetics. *Corros. Sci.* **90**, 375–382 (2015).

45. Zamanzade, M., Shahrabi, T. & Yazdian, A. Improvement of corrosion protection properties of calcareous deposits on carbon steel by pulse cathodic protection in artificial sea water. *Anti-Corros. Methods Mater* **54**, 74–81 (2007).

46. GB/T, Sacrificial anode of Al-Zn-In series alloy. https://www.doc88.com/p-6857792534359.html.

47. Long, X., Fang, X., Mei, Y., Fan, Z. & Zhang, W. Electrochemical Performance of Al-Zn-In-Si Sacrificial Anode in Simulated Seawater and Sea Mud Environment. *Surf. Technol.* **50**, 297–305 (2021).

48. Wang, W., Zhang, X. & Wang, J. The influence of local glucose oxidase activity on the potential/current distribution on stainless steel: A study by the wire beam electrode method. *Electrochim. Acta.* **54**, 5598–5604 (2009).

ACKNOWLEDGEMENTS

AUTHOR CONTRIBUTIONS

C.Y.: Investigation, Writing—original draft. X.W.: Methodology, Writing—original draft. W.Z.: Conceptualization, Methodology, Writing—review and editing, Visualization, Supervision, Funding acquisition. W.X.: Methodology, Resources. Z.C.: Verification, Supervision. Bing Han: Verification, Supervision.

COMPETING INTERESTS

The authors declare no competing interests.

ADDITIONAL INFORMATION

Correspondence and requests for materials should be addressed to Wei Zhang.

Reprints and permission information is available at http://www.nature.com/reprints

Publisher's note Springer Nature remains neutral with regard to jurisdictional claims in published maps and institutional affiliations.